SpuBase: Solar Wind Ion Sputter Database for Modeling Purposes

Noah Jäggi[1,2] , Herbert Biber[3] , Johannes Brötzner[3] , Paul Stefan Szabo[4] , Andreas Mutzke[5], Jonathan Gasser[1] ,
Friedrich Aumayr[3] , Peter Wurz[1] , and André Galli[1]
[1] Space Science and Planetology, Physics Institute, University of Bern, Sidlerstrasse 5, CH-3012 Bern, Switzerland; noah.jaeggi@unibe.ch
[2] Material Science and Engineering Department, University of Virginia, 395 McCormick Road, Charlottesville, VA 22904, USA
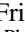[3] Institute of Applied Physics, TU Wien, Wiedner Hauptstraße 8-10/E134, A-1040 Vienna, Austria
[4] Space Sciences Laboratory, University of California, 7 Gauss Way, Berkeley, CA 94720, USA
[5] Max Planck Institute for Plasma Physics, Wendelsteinstraße 1, DE-17491 Greifswald, Germany
Received 2023 November 17; revised 2024 January 30; accepted 2024 February 13; published 2024 March 21

Abstract

We supply the modelers with a database, SpuBase (doi:10.5281/zenodo.10783295), that is based on the latest approach for obtaining solar wind ion sputter yields in agreement with experimental sputter data outlined in Jäggi et al. We include an overview of sputter results for typical Lunar and Hermean surfaces. To obtain total sputter yields for any given surface, we perform a mass balance of individual mineral sputter yields. For a set of impact angles, the angular and energy distribution data are scaled according to the sputter yield, summed up and fitted to obtain one probability distribution for each chemical element involved. Comparison of the results from different geochemical terranes on the Moon and Mercury has shown that variations in the abundance of silicates result in comparable energy and angular distribution data owing to the underlying model assumptions. The inclusion of sulfides relevant for Mercury, however, significantly affects the energy and angular distributions of sputtered particles. The application of the damage-driven sulfur diffusion rate in FeS in all sulfur-bearing minerals results in 35 times lower sulfur yields on average and a less prominent forward sputtering of sulfur at grazing incidence angles.

Unified Astronomy Thesaurus concepts: Solar wind (1534); Exosphere (499); Mercury (planet) (1024); The Moon (1692); Asteroids (72)

1. Introduction

Solar wind (SW) ion sputtering (IS) is one of two major processes that supply refractory atoms with suprathermal velocity distributions to the Lunar and Hermean exosphere. At Mercury, micrometeoroid fluxes are enhanced, and thus IS competes with micrometeoroid impact vaporization (Killen et al. 2022; Wurz et al. 2022) at cusp and auroral regions (e.g., Pfleger et al. 2015) and under extreme conditions over Mercury's dayside (e.g., Winslow et al. 2020). To determine the importance of weathering processes for the chemistry and structure of the exosphere, supply rates and the properties of the ejected material have to be constrained. Based on the latest experimental and computational work (Jäggi et al. 2023), we study the variation in sputter yields of different mineral groups and establish a database (SpuBase, doi:10.5281/zenodo.1078329, Jäggi 2024, Appendix A) that holds sputter yields and particle information that best represents the laboratory data available at the time of writing.

Surfaces exposed to the SW are strongly weathered and become significantly altered in the process. Lunar regolith expresses this in the form of an amorphous layer surrounding grains (Heiken et al. 1991; Domingue et al. 2014), abundant agglutinates and glass components (Betz & Wien 1994; Loeffler et al. 2009; Dukes et al. 2011; Domingue et al. 2014), and reduction of Fe into nanophase iron (e.g., Housley et al. 1973; Taylor et al. 2001). The proximity of Mercury to the Sun and the increased importance of impacts in regolith

formation are considered to be responsible for increased melt (∼13×) and vapor (∼19.5×) production compared to the Moon, leading to a presumably higher amount of agglutinates and glass (Cintala 1992; Pieters & Noble 2016).

The quantity and properties of particles released from complex regolith surfaces by IS are required by exosphere−magnetosphere models in the hope of recreating observations of the surroundings of space-weathered bodies. For a long time, TRIM (Ziegler et al. 2010) was widely used to obtain sputter yields for a flat surface with a bulk composition equal to the approximate planetary body composition (e.g., Wurz et al. 2010). There have since been advances in sputtering simulations, including 3D simulations, taking into account porosity and roughness of surfaces (e.g., Szabo et al. 2022b; Biber et al. 2022). There have not been new holistic approaches that cover all elements sputtered, however, since models and codes became increasingly capable but also cumbersome and computationally demanding. In this work, to simulate the sputtering of regolith grains, the Monte Carlo binary collision approximation model SDTrimSP is used. The use of SDTrimSP has been made more accessible by the recent addition of a graphical user interface (Szabo et al. 2022a). Nevertheless, the knowledge, time, and resources needed to simulate sputtering of a surface in SDTrimSP—or complex surfaces in SDTrimSP-3D (von Toussaint et al. 2017)—still pose a daunting challenge to modelers who require input for their exosphere models. This fact is well illustrated in Morrissey et al. (2023), where many parameter choices and their historic applications are outlined. With this publication, we provide a database for those users who are eager to work with the state-of-the-art results verified with laboratory

measurements (Jäggi et al. 2023) without being required to run complex sputter models.

To approximate the IS of regolith grains, this work combines the model data of 21 major rock-forming minerals for simulated 1 keV H and 4 keV He impacting ions, i.e., kinetic energies corresponding to a median SW speed of about 440 km s^{-1} (Gosling 2007). The database is applicable to the Moon, Mercury, and any rocky body irradiated by H and He ions with typical SW speeds in proximity to the Sun. The database was produced with the new hybrid binding energy compound model (HB-C; Jäggi et al. 2023) for the SDTrimSP code. The new HB-C model reached a good agreement with laboratory data using

1. dynamic computations, which cause the surface to be altered to the point of reaching an equilibrium in surface composition, as well as constant sputter yields;
2. properly prescribed mineral densities based on tabulated data of metal oxides and sulfur-bearing compounds; and
3. increased binding energy based on the enthalpy of formation required to break up bonds in a compound, strongly affecting the energy and angular distribution of the sputtered particles.

The effects of the surface positions of atoms and the crystal lattice of the irradiated mineral are not considered in the HB-C model but are important for pristine samples. The regoliths of the Moon and Mercury are, however, mostly composed of glass, and the regolith grains express a glassy surface layer, therefore making lattice information negligible. Biber et al. (2022) convincingly illustrate how the yield difference between an amorphous thin film and a rough, crystalline pellet of the same composition can be explained solely by the surface roughness. No significant effect of the crystalline structure was found in these experiments. The data in SpuBase therefore only apply to sputter yields from weathered surfaces.

With an average of 20 computations per mineral and more than 420 computations, we present a database capable of saving the user hundreds of hours of computation time while reproducing over 30 GB of raw output data stored within less than 3 MB. The data are then accessed by a lightweight Python package to determine elemental sputter yields of chemically complex surfaces, including the angular and energy distributions of sputtered particles as a function of incidence angle. SpuBase significantly improves on the widely used TRIM (Ziegler et al. 2010) to obtain sputter data by reproducing data created by the latest SDTrimSP model with hitherto unprecedented agreement with the few existing laboratory data.

2. Methods of Computation

The computation of the results in SDTrimSP and TRIM follows the settings used in Jäggi et al. (2023) and uses only the compound hybrid binding energy model (HB-C) in the SDTrimSP computations. We briefly summarize the model assumptions here, but we refer the reader to Jäggi et al. (2023) for an in-depth description.

Any atom in a pristine mineral starts off as a bound species within a compound. To remove the species from the compound, a bulk binding energy according to a fraction of the compound enthalpy of formation has to be overcome. Only monatomic species are included as unbound species, but they are allowed to reform their original compounds. If a species reaches the sample surface, it further has to overcome a surface

binding energy, approximated by its energy of sublimation, unless the species is a gas under standard conditions. The density of the sample and therefore the mean free path within the sample are calculated from the atomic densities of the compound and the unbound species present. The combination of surface binding energies and connecting both bulk binding energies and densities to known mineral properties makes the HB-C model a favorable approach without the need of fitting to experimental data.

The data included in SpuBase are limited to flat surfaces. How surface roughness affects sputter yields is shown in Biber et al. (2022). Extensive calculations taking into account the effects of roughness and porosity are still a work in progress. The flat surface data could then be introduced into porosity and roughness models (Küstner et al. 1998; Cupak et al. 2021) to determine the yields and angular distributions of particles emitted from any rough surface. This capability of 3D models to recreate sputter yields of a rough surface from 1D SDTrimSP data was demonstrated in Biber et al. (2022). To best represent a regolith surface, the data from SpuBase would have to be applied to a regolith model in order to reproduce effects of regolith porosity, roughness, and grain size distribution. The nanometer scale of the sputtering process makes the flat surface applicable to the micron scale of typical regolith grains and any larger constituents, however.

2.1. Minerals Included in SpuBase

The data in SpuBase cover single minerals being irradiated by one of the two major SW ion species at a time. We motivate the use of single minerals with two arguments. First, passing the complete composition of a regolith of interest at once to SDTrimSP bears the issue of relative element abundances. Two distinct elements express (1) different mass and therefore potentials; (2) different energy loss between collisions, i.e., inelastic energy loss or electronic loss; and (3) different binding energies.

The absolute and relative element proportions thus affect collision behavior and energy transfer, resulting in variations in the elemental sputter yield and the energy and angular distributions of sputtered particles on a microscopic level. Computing a complex composition such as regolith as one single amorphous sample is thus evidently problematic. For example, the abundance of minor elements such as Na varies strongly between the mineral albite (7.7 at%) and a typical lunar Highland anorthosite rock (0.35 at%; Table 2). Distinguishing the origin of sputtered particles from chemically different sources that make up a large surface is necessary, and in this work we do so in approximating said surface with major rock-forming minerals.

A second motivation for approximating regolith with single minerals is that even if grain sizes in regolith become small (averaging about 100 μm; Heiken et al. 1991), sputtering by SW still operates on nanometer depth scales, where the released atoms originate from the top few atomic layers. For rock-forming minerals, average SW speed He ions penetrate $\sim$30 nm (e.g., Jäggi et al. 2021). Hence, each regolith grain can be treated as a single sample. We expect that distinct grains have been altered to the point where treating them as minerals in equilibrium with the SW is a good approximation. Furthermore, in SDTrimSP an amorphous sample is assumed and no differentiation for crystalline samples is possible in the model. This is not a shortcoming in our case, as (1) there is a

Table 1
Major Rock-forming Minerals Required to Represent an Unknown Planetary Surface and Their Densities

Group	Mineral		Formula	ρ_{ref} (g cm^{-3})	ρ_{ref} (at/Å^3)	ρ_{cpd} (g cm^{-3})	ρ_{cpd} (at/Å^3)	$\Delta\mu_{\mathrm{cpd}}$ (1)	ρ_{atm} (g cm^{-3})	ρ_{atm} (at/Å^3)	$\Delta\mu_{\mathrm{atm}}$ (1)
Feldspar	Orthoclase	Or	KAlSi$_3$O$_8$	2.56	0.0723	2.67	0.0754	−1%	1.36	0.038	23%
	Albite	Ab	NaAlSi$_3$O$_8$	2.62	0.0786	2.70	0.0808	−1%	1.43	0.043	22%
	Anorthite	An	CaAl$_2$Si2O$_8$	2.73	0.0768	2.99	0.0840	−3%	1.53	0.043	21%
	Nepheline	Nph	NaAlSiO$_4$	2.59	0.0747	2.84	0.0820	−3%	1.44	0.041	22%
Pyroxene	Wollastonite	Wo	CaSiO$_3$	2.93	0.0760	2.91	0.0755	0%	1.45	0.038	26%
	Diopside	Di	CaMgSi$_2$O$_6$	3.40	0.0946	2.97	0.0827	5%	1.46	0.041	33%
	Enstatite	En	Mg$_2$Si$_2$O$_6$	3.20	0.0960	3.05	0.0913	2%	0.74	0.044	29%
	Ferrosillite	Fs	Fe$_2$Si$_2$O$_6$	3.95	0.0902	3.82	0.0872	1%	1.08	0.049	22%
Olivine	Forsterite	Fo	Mg$_2$SiO$_4$	3.27	0.0980	3.21	0.0960	1%	1.46	0.044	31%
	Fayalite	Fa	Fe$_2$SiO$_4$	4.39	0.0908	4.64	0.0900	0%	2.48	0.051	21%
Oxides	Ilmenite	Ilm	FeTiO$_3$	4.72	0.0937	4.83	0.0959	−1%	1.58	0.047	32%
	Quartz	Qz	SiO$_2$	2.65	0.0797	2.65	0.0797	0%	2.88	0.054	18%
Sulfides	Troilite	Tro	FeS	4.61	0.0632	4.61	0.0632	0%	2.54	0.050	23%
	Niningerite	Nng	MgS	2.68	0.0573	2.68	0.0573	0%	1.51	0.046	21%
	Alabandite	Abd	MnS	3.99	0.0552	3.99	0.0552	0%	3.89	0.053	6%
	Brezinaite	Bzn	Cr$_3$S$_4$	4.12	0.0611	4.23	0.0629	−1%	1.91	0.041	12%
	Wassonite	Was	TiS	3.85	0.0580	3.85	0.0580	0%	3.80	0.053	2%
	Oldhamite	Old	CaS	2.59	0.0432	2.59	0.0432	0%	1.74	0.029	14%
	Daubréelite	Dbr	FeCr$_2$S$_4$	3.81	0.0557	3.41	0.0570	−1%	3.07	0.046	8%
Accessories	Spinel	Sp	MgAl$_2$O$_4$	3.64	0.1078	3.77	0.1115	−1%	3.40	0.050	7%
	Chromite	Chr	FeCr$_2$O$_4$	4.79	0.0902	5.29	0.0996	−3%	3.25	0.048	5%

Note. Differences in mean free path lengths ($\mu = \rho^{-1/3}$) are calculated as $\Delta\mu = \mu/\mu_{\mathrm{ref}} -1$. Short forms: ρ_{ref}—mass densities and atomic densities calculated based on typical mineral densities found on http://webmineral.com (e.g., Deer et al. 1992); ρ_{cpd}—densities calculated based on tabulated compound data based on pure compound properties; ρ_{atm}—densities calculated based on atomic data included in tables of SDTrimSP, which are based on monoatomic solids.

significant abundance of glass rims on grains, glass, and agglutinates observed in lunar regolith grains (Heiken et al. 1991; Domingue et al. 2014), suggesting an overall amorphous interaction surface; and (2) no significant effect of crystallinity on sputter yields for mineral grains has been reported in experiments, which is likely tied to the rapid amorphization of the uppermost monolayers of the surface grains (Biber et al. 2022).

Based on these arguments, we approximate bulk surface compositions by the major rock-forming minerals shown in Table 1. We simulate particles that originate from well-defined minerals. The result of the whole rock is a weighted average of the results from the individual minerals instead of doing the simulation for the averaged elemental abundances. If just the elemental composition is known, we use an adapted Cross−Iddings−Pirsson−Washington (CIPW) norm (Cross et al. 1902) to allocate elements into minerals (Section 2.6).

2.2. Diffusion within Sulfides

Christoph et al. (2022) have shown that troilite (FeS) irradiated by SW energy He$^+$ and H$^+$ is rapidly depleted in sulfur, based on in situ X-ray photoelectron spectroscopy (XPS) measurements. The degree of the observed S depletion in the top <10 nm was related to enhanced mobilization to the surface by damage-driven diffusion. In SDTrimSP, the mobilized S can then leave the sample without being sputtered, contributing to S ejected at thermal energies. Diffusion thus becomes the dominant process of S removal from the sample in the model, which is unlikely to be the case in laboratory experiments. In any case, we expect diffusion to be efficiently reducing the total sputter yield of S from any surface that comprises S-bearing minerals in addition to reducing the energy of ejected S species.

For diffusion cases, the HB-C model is adjusted (HB-CD) to prevent sulfur and metal atoms from reforming their initial sulfide bonds, instead forming the reduced, monatomic species. For example, if a FeS compound is broken up into unbound Fe and S, the atoms are considered to remain unbound and do not reform the original FeS. The motivation for this was that the default HB-C model prevents compound-bound species to be mobilized in any way.

In SDTrimSP diffusion is defined as a function of fluence because there is no time information available (Mutzke et al. 2019). The fluence-dependent diffusion is defined as

$$\frac{\delta n}{\delta \phi} = -\frac{\delta\left(\eta(z)\frac{\delta n(z)}{\delta z}\right)}{\delta z}, \qquad (1)$$

with the number density n, the fluence ϕ, the depth z, and the diffusion coefficient η. The damage-driven diffusion as a function of depth is calculated as

$$\eta(z) = \eta_0 \, P_{\mathrm{dam}}, \qquad (2)$$

with the maximum diffusion rate of η_0 and the relative probability for diffusion as a function of damage P_{dam}. The diffusion probability is calculated as

$$P_{\mathrm{dam}} = \frac{N_{\mathrm{dam}}}{\max[N_{\mathrm{dam}}]} qu(z), \qquad (3)$$

with the number of damaged lattice sites N_{dam} and the atomic abundance of the species at depth z as $qu(z)$. The value of η_0 for sulfur in troilite (FeS) at ambient temperature was constrained to 7.5×10^2 Å^4 ion^{-1} (Christoph et al. 2022). The equivalent diffusion coefficient that Christoph et al. (2022) found given their flux and fluence was 5.6×10^{-22} cm^2 s^{-1} at 300 K.

Due to a lack of diffusion coefficients for the other S-bearing species included in SpuBase, we used the damage-driven diffusion coefficient of S in troilite for all minerals. Given the high dayside surface temperatures of Mercury (700 K; Hale & Hapke 2002; Paige et al. 2013), the effect of temperature on the diffusion could be significant, but no laboratory data are available that constrain a possible temperature dependency. Christoph et al. (2022) also considered implantation of H and He within the sulfide; however, they did not disclose the density diffusion coefficient of either species to reproduce their results. Implantation was thus neglected in our computations. The effect of impactor implantation on the surface depletion of S is expected to be marginal (Appendix B), as the implantation of impactors does not exceed 0.16 at% (according to Figure 8 in Christoph et al. 2022).

2.3. Implantation, Diffusion, and Ejection of Solar Wind Ions

The implantation and diffusion of impactors (H/He) are not considered in SpuBase. The reason is twofold: (1) there is a lack of experimental data on H and He implantation in the minerals listed in Table 1, and (2) the model used (Jäggi et al. 2023) reproduces mass yields well, suggesting a negligible amount of implantation (implanting light species would significantly decrease the mass of ejected particles). The diffusion process is suggested to be damage-driven and temperature dependent as modeled in Farrell et al. (2015) and could be included similar to sulfur diffusion as soon as reference measurements are available. In the meantime, no implanted H/He is sputtered, and therefore it is not present in the results, although we would expect it to be.

2.4. Impactor Composition

To enable validation of the SpuBase data with experiments, data from H and He impactors are included separately in addition to the default SW impactor data. To obtain results for SW irradiation that deviate from the default composition (96% protons and 4% alpha particles; Aellig et al. 2001; Gosling 2007), the SpuBase sputter yields for each mineral are mass balanced according to the chosen SW composition. The combined particle angular and energy distributions are determined by a sum product of the respective element yield for both H and He and refitted with Equations (4)–(8).

2.5. Fitting the Simulated Data

For each mineral, an SDTrimSP simulation is run at 23 incidence angles between 0° and 89°. Below 45° from the surface normal, the step size is 10°. From 45° onward the step size is decreased to 3° before being further decreased to 2° above 72°.

For each incident angle, several output files are generated by SDTrimSP with sizes ranging from a few MB for the sputter yield and surface data to hundreds of MB for particle trajectory information. To reduce the data volume for fast and efficient access, it is necessary to have an analytic description, which we derive from fitting the data. Well-established fit functions from the literature are applied to best conserve the information from the SDTrimSP results. The equations follow the fit functions used in Jäggi et al. (2023) with the addition of a normalization factor k_ϕ for the angular fit function and both k_E and a cutoff energy E_{bc} in the energy fit function (Wurz & Lammer 2003). The normalization factor k is the integrated area of the fit

function and transforms the angular and energy fits into probability density functions.

For the sputter yield, a single fit is sufficient to express the results at all incidence angles. This does not apply to the angular and energy distributions, which require a set of fit parameters for each incidence angle. To get a better-resolved description of the angular and energy distributions, their respective parameters were linearly interpolated at a step size of 1° between the 21 available data points. We motivate this with the small step size at incident angles with large changes in fit parameters ($\alpha > 45°$) and the small changes observed close to normal incidence ($\alpha < 45°$).

The modeled sputter yield is fitted using an Eckstein fit (Eckstein & Preuss 2003):

$$Y(\alpha; b, c, f) = Y_0 \{\cos \alpha^c\}^{-f}$$
$$\times \exp\left\{ b\left(1 - \frac{1}{\cos \alpha^c}\right)\right\}, \quad (4)$$

with $Y_0 = Y(\alpha = 0)$; the fitting parameters b, c, and f; and the angle of incidence α.

For the angular distribution of sputtered particles, the data are fitted using an adapted cosine fit function (Hofsäss & Stegmaier 2022) to take the nonsymmetrical nature of sputtered particles into account. The angular fit function is as follows:

$$f(\phi) = \frac{1}{k_\phi}\begin{cases} \cos^m\left(\frac{\pi}{2}\left(\frac{\pi + 2\phi}{\pi + 2\phi_{\text{tilt}}} - 1\right)\right) & \phi \leqslant \phi_{\text{tilt}} \\ \cos^n\left(\frac{\pi}{2}\left(1 - \frac{\pi - 2\phi}{\pi - 2\phi_{\text{tilt}}}\right)\right) & \phi \geqslant \phi_{\text{tilt}} \end{cases}$$
$$\text{with } k_\phi = \int_{\phi=0}^{\pi} f(\phi, \phi_{\text{tilt}}, m, n)\, d\phi, \quad (5)$$

with the tilt angle of the distribution maximum ϕ_{tilt} relative to the surface normal, the normalization factor k_ϕ, and the ejection angle ϕ.

The energy distribution data are typically represented by a normalized Thompson distribution (Thompson 1968),

$$f(E; E_0) = \frac{1}{k_E}\frac{E}{(E + E_0)^3}$$
$$\text{with } k_E = \int_{E=0}^{\infty} f(E; E_0) = \frac{1}{2\,E_0}dE, \quad (6)$$

with the energy of the sputtered atom E, the normalization factor k_E, and a characteristic binding energy E_0 that describes the energy removed from the sputtered atom before it escapes the sample. The energy peak is located at $E_0/2$ in Equation (6). In this work we use the adapted Thompson fit function (Wurz & Lammer 2003) instead, which is

$$f(E; E_0) = \frac{1}{k_E}\frac{E}{(E + E_0)^3}\left(1 - \sqrt{\frac{E + E_0}{E_{BC}}}\right)$$
$$\text{with } k_E = \int_{E=0}^{\infty} f(E, E_0)dE, \quad (7)$$

where the cutoff term includes the maximum energy, E_{BC}, that can be transferred in a binary collision resulting from an

impactor with energy E_{in}:

$$E_{BC} = E_{in} \frac{4m_{ion}m_{surf}}{(m_{ion} + m_{surf})^2}. \tag{8}$$

2.6. Adapted CIPW Norm for Surface Compositions

To pass a surface composition to SpuBase, the modal abundances (in vol%) of minerals are required. Alternatively, the oxide or atomic composition can be passed if the mineralogy of the surface is not known or is not available in terms of major rock-forming minerals.

To allocate any given composition into minerals, we use an adapted CIPW norm (Cross et al. 1902) based on the approaches in Vander Kaaden & McCubbin (2016) and McCoy et al. (2018). The CIPW norm does not rely on thermodynamic data, but instead relies on known relations of rocks and minerals, an assumed order of mineral formation, and simplified mineral formulae. This issue was addressed in Section 2.1, where we argue that the minerals represent a glassy surface, which better describes volcanic rocks.

The CIPW norm is applicable only for single igneous units and under terrestrial oxygen fugacity conditions. To address this, minor elements such as Fe, Mn, Cr, and Ti were assigned to sulfides (McCoy et al. 2018). Both limitations are generally not met on Mercury. As a consequence, none of these transition elements occur as oxides, as experimentally shown by Vander Kaaden & McCubbin (2016). As a result, the CIPW norm can be applied after redox-sensitive elements such as Fe have been removed.

The adapted implementation of the CIPW norm (Cross et al. 1902) into SpuBase thus reads as follows:

1. If sulfur is present, the composition must be passed on as elements, as Mn, Cr, and Ti are attributed to sulfides, followed by Fe, as observed in experiments by Vander Kaaden & McCubbin (2016) and applied by Vander Kaaden & McCubbin (2016) and McCoy et al. (2018). If any S is left, Mg and Ca are attributed to sulfides in a ratio of 3:1 (Weider et al. 2012, 2015; Vander Kaaden & McCubbin 2016; McCoy et al. 2018). The remaining elements are then converted into oxides, ignoring the limited O availability as in McCoy et al. (2018).
2. Diopside (Ca[Mg, Fe]Si$_2$O$_6$) is divided into a ferrosilite (FeSiO$_3$) and a pure Mg-diopside (CaMgSi$_2$O$_6$) component. Leftover CaO is attributed to a wollastonite component (CaSiO$_3$) unless the lack of SiO$_2$ can be negated by forming olivine ([Mg, Fe]$_2$SiO$_4$) and/or nepheline (Na$_3$KAl$_4$Si$_4$O$_{16}$, a feldspatoid formed by removing one SiO$_2$ from albite) instead.
3. Olivine ([Mg, Fe]$_2$SiO$_4$) is separated into its end-members forsterite (Mg$_2$SiO$_4$) and fayalite (Fe$_2$SiO$_4$).

The obtained molar mineral composition is then used for further SpuBase calculation. To validate the CIPW results, the molar mineral abundances are divided by their molar mass and normalized to unity. Albite and anorthite are summed up and reported as plagioclase, whereas the diopside, olivine, and orthopyroxene (or hyperstene) results that were separated into components are reported, allowing for a direct comparison with the default CIPW norm.

3. Results

We first present an overview of simulated MgSiO$_3$ sputter results in normalized mass yields, calculated from the sum product of element yields and their respective atomic mass (Figure 1). This choice is due to the lack of experimental angular distribution data for rock-forming minerals (Biber et al. 2022) and a clear illustration of tendencies. For all minerals, we find that the tilt angle and the shape parameters m and n reach their maximum for an incident angle α_{in} of 60°–70°. It is in question whether or not the forward-facing peak is a modeling artifact. For example, Wilhelm et al. (2023) showed an absence of the characteristic, forward-facing single collision peak in experimental data of 14 keV Sn$^+$ backscattered from a Mo surface. If the single collision peak is a simulation artifact, the residuals of the fit shown in Figure 1 for grazing incidence angles would be significantly reduced.

Typical energy distributions for minerals in the database are shown in Figure 2 for normal and grazing angles of incidence. The change in characteristic binding energy E_0 ($E_0 \approx 2E_{peak}$) as a function of incidence angle is given in Figure 3. Energy distributions of all minerals retrieved from the HB-C model follow a similar trend, and E_0 remains constant for a wide range of incidence angles ($\alpha_{in} \leqslant 80°$). All results in Section 3 are for average SW conditions with 96% H$^+$ and 4% He^{2+} and 440 km s^{-1} SW speed. Changing the ion impact speed to reflect slow or fast SW has minor effects on the sputtering results (see Appendix C for more details). Under extreme conditions, the increases in yields are expected to be significant and reach up to three orders of magnitude between the typical SW and a coronal mass ejection driver gas composed of 70% H$^+$ and 30% He^{2+} with a density of 70 ions cm^{-2} and a velocity of 500 km s^{-1} (Killen et al. 2012), which corresponds to an order-of-magnitude-higher SW density and He^{2+} abundance.

3.1. SpuBase Demonstration

The result of combining single mineral atomic sputter yields, angular distributions, and energy distributions is shown in Figures 4 and 5 for lunar and Hermean regolith compositions, respectively. Azimuth angle information is not included in the database but shown in Appendix D. The chosen compositions are averages of lunar highlands (anorthosite) and Mare, and for Mercury with the average surface composition, represented by the Southern Hemisphere, and the largest of the geochemical terranes, the northern low-Mg terrane (Table 2; Heiken et al. 1991; McCoy et al. 2018; Peplowski & Stockstill-Cahill 2019). The resulting element-specific binding energies E_0 for the different Lunar and Hermean surfaces are given in Table 3 and are compared to the surface binding energies used in Wurz et al. (2010) and to the tabulated enthalpy of sublimation (E_s) of each element.

3.2. Sulfides and Diffusion

The data for Mercury include sulfides, whereas the lunar regolith is largely devoid of S-bearing minerals. The effect on S sputtered in equilibrium from a heavily S-depleted sulfide is shown in Table 4. The removal of S causes an accumulation of the secondary element, which can strongly increase the total mass yield from these surfaces. This is illustrated by the difference in erosion rates from sulfides with and without diffusion compared to enstatite (Table 5).
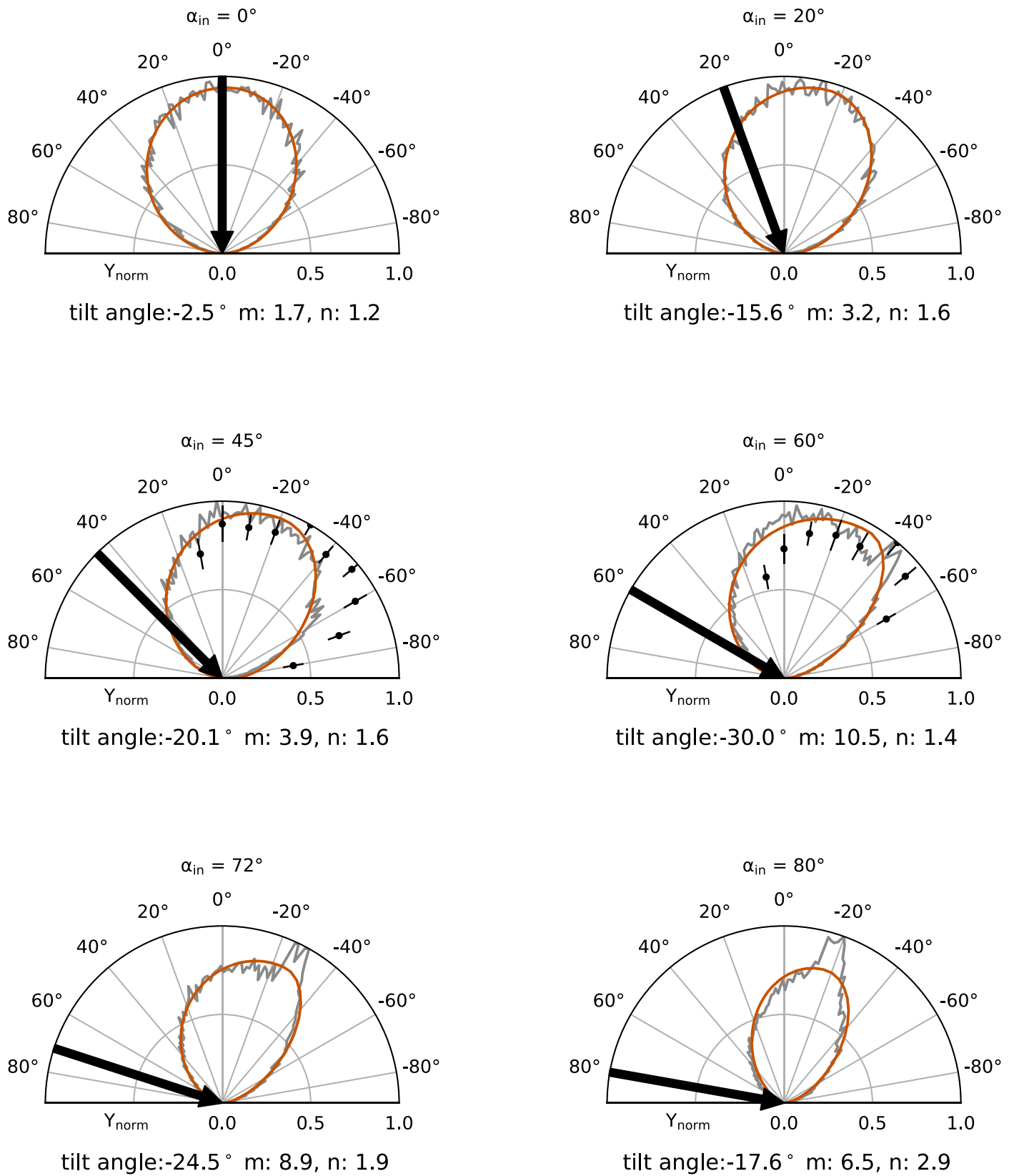
Figure 1. Polar angular distribution of normalized mass yield Y_{norm} sputtered from enstatite ($MgSiO_3$) by 4 keV He^+ at increasing incident angles (α_{in}) compared to experimental data (black; Biber et al. 2022) with errors of 2 standard deviations.

For example, for troilite the depletion causes about 30% and 12% lower peak energies in the energy distribution of sputtered S and Fe, respectively. The angular distribution of the sputtered S is also strongly affected in the damage-driven diffusion case, where the plume of sputtered S does not exceed forward tilt angles of 28° compared to the 38° in the case without diffusion.
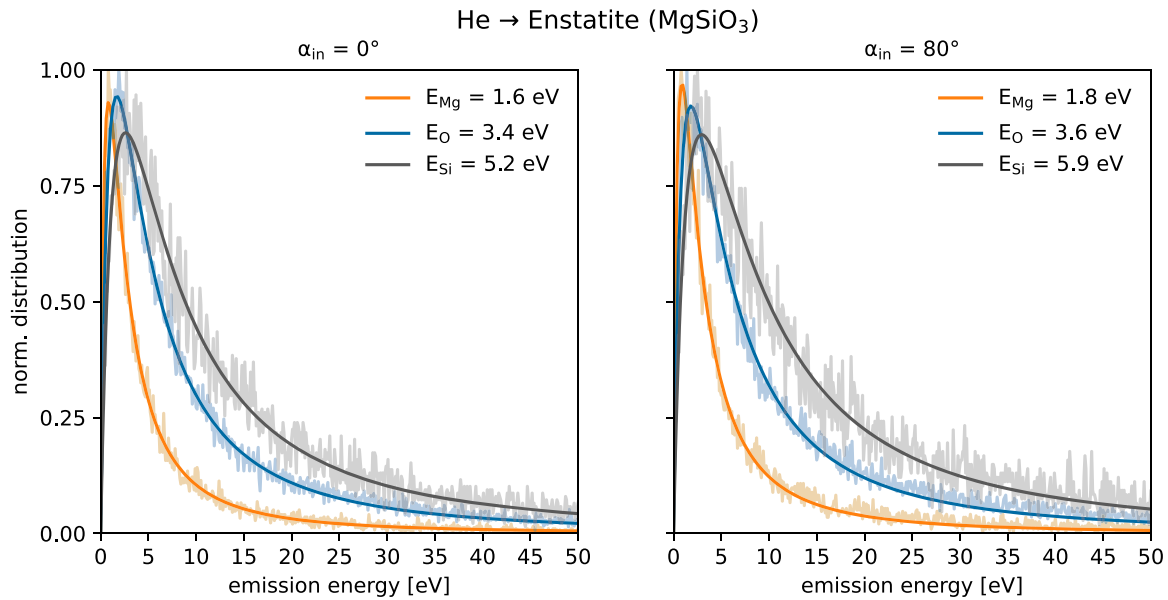
Figure 2. Energy distribution of particles sputtered from enstatite (MgSiO$_3$) irradiated by He ions at normal incidence $\alpha_{in} = 0°$ and at $80°$ with respect to the surface normal. The legend contains the element-specific characteristic binding energy E_0, whereas $E_0 \approx 2E_{peak}$.
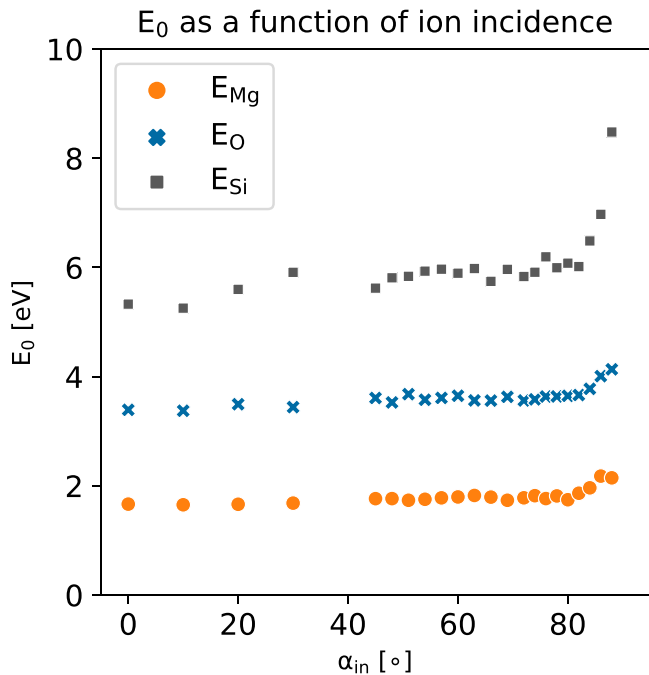
Figure 3. Characteristic energy E_0 of the energy distributions of particles sputtered from enstatite (MgSiO$_3$) irradiated by He ions at incident angles α_{in}. For all species the E_0 is nearly constant but increases rapidly at grazing incident angles $\alpha_{in} > 80°$.

The maximum forward tilt for Fe is not significantly affected and only reduced by ~2% in the diffusion case. This trend also applies to the other sulfides listed in Table 1 because the same diffusion rate was chosen for all sulfides (Section 2.2). This is due to the nonnegligible contribution of sputtered particles that originate from below the reduced uppermost sample layers.

The adapted model ($Y_{HB\text{-}CD}$) results in identical atomic sputter yields to the "default" surface binding model with diffusion (default model yields not shown, as it overlays with HB-CD; Figure 6), while reproducing the ideal mineral

Table 2
Elemental Compositions in wt% for Typical Lunar and Hermean Surfaces

| | Moon | | Mercury | |
	Apollo 11 Mare Basalt	Highland Anorthosite	Southern Hemisphere	Northern Low-Mg Terrane
O	41.81	45.47	39.65	42.93[a]
Na	0.28	0.35	2.83	5.83
Mg	4.23	0.73	12.44	6.13
Al	5.33	17.68	7.79	4.60
Si	18.91	21.30	28.32	30.67
S	1.94×10^{-3}	0.00	2.07	2.15
Cl	1.35×10^{-5}	0.00	0.14	0.43[b]
K	5.40×10^{-4}	1.23×10^{-4}	0.13	0.18
Ca	8.25	13.65	4.55	4.60
Ti	6.24	0.05	0.34	1.07[c]
Cr	2.09×10^{-3}	0.00	0.14	0.02[d]
Mn	1.92×10^{-3}	0.00	0.11	0.11[e]
Fe	14.94	0.78	1.48	1.84
Total	100.01	100.00	99.99	100.02
Ref	H91	H91	M18	P19

Notes. Lunar highland is represented by anorthosite (Heiken et al. 1991) and Mercury's average composition by the southern hemisphere composition (McCoy et al. 2018).
[a] Evans et al. (2012).
[b] Evans et al. (2015).
[c] Cartier et al. (2020).
[d] Nittler et al. (2023).
[e] Weider et al. (2014).
References. H91—Heiken et al. (1991); M18—McCoy et al. (2018); P19—Peplowski & Stockstill-Cahill (2019).

densities and increased binding energies within the less altered, deeper layers within the irradiated sample. We expect nontroilite sulfides to express a comparable diffusion. The resulting data for all sulfides with a damage-driven diffusion enabled are comparable to troilite.
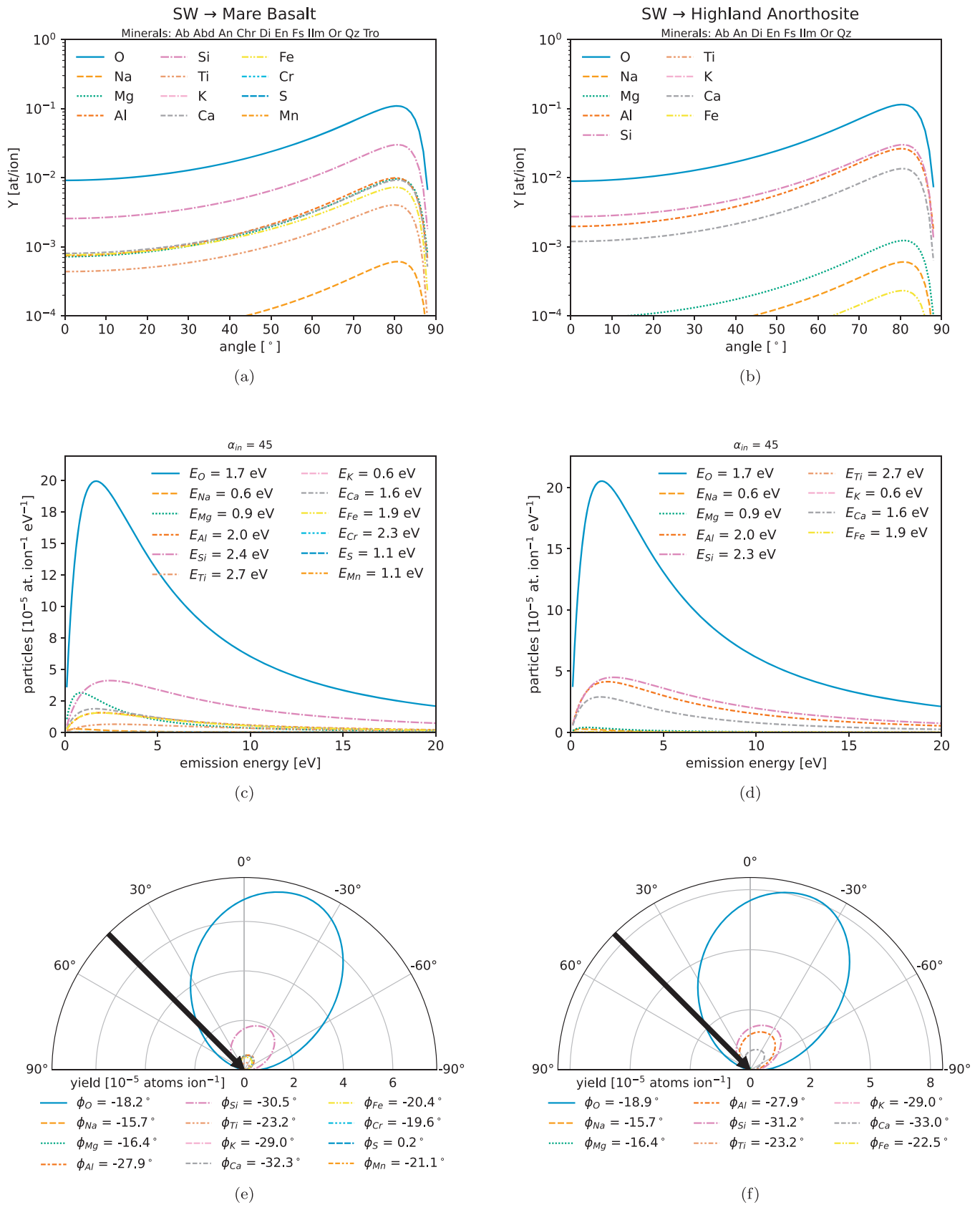
Figure 4. SW IS data for a typical Lunar mare and Lunar highland composition (Heiken et al. 1991). Energy and angular distributions are shown for an incident angle of 45°.
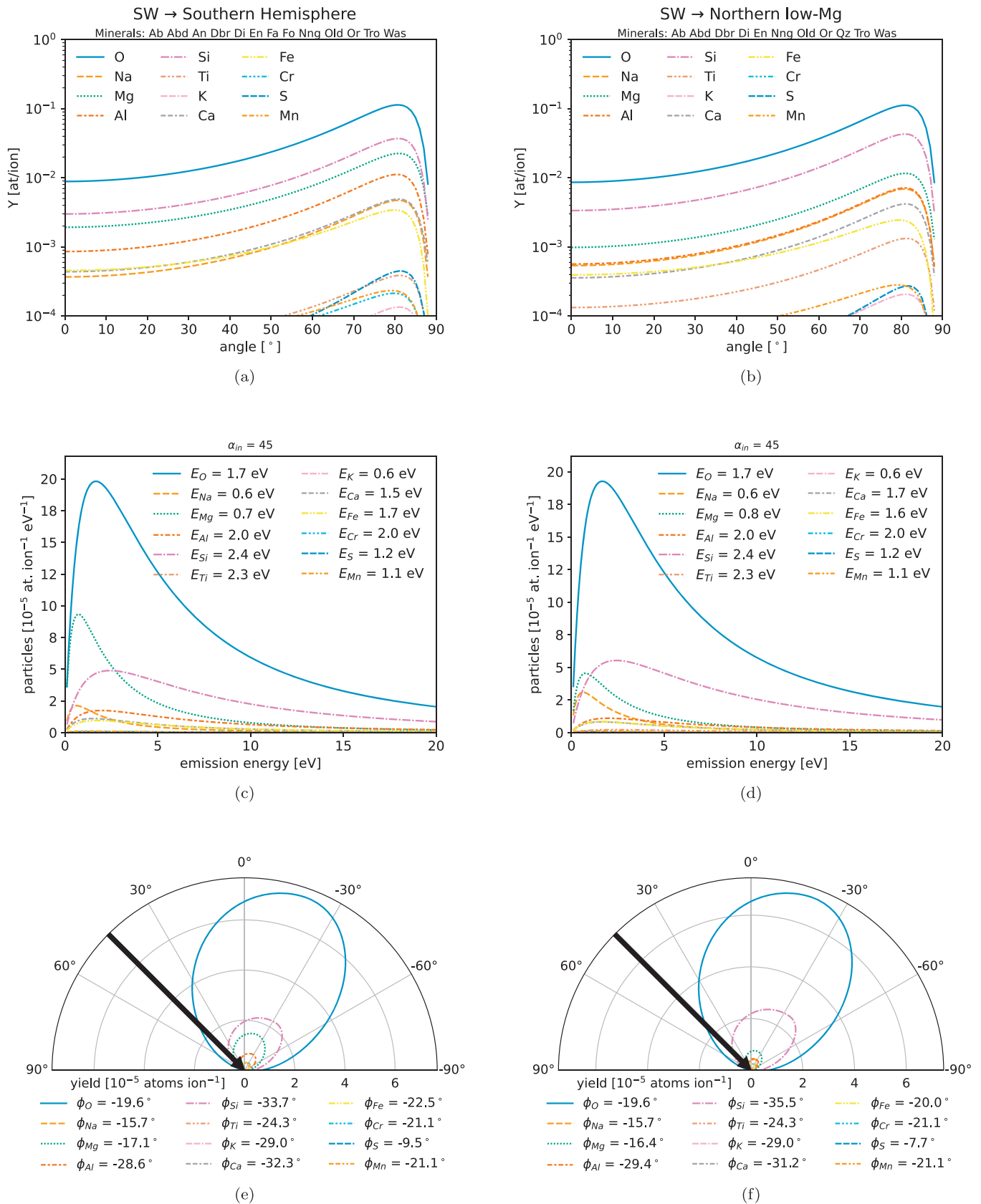
Figure 5. SW IS data for Mercury's southern hemisphere and northern low-Mg composition from McCoy et al. (2018) and Peplowski & Stockstill-Cahill (2019), respectively (Table 2). Energy and angular distributions are shown for an incident angle of 45°.

Table 3
Comparison between the Tabulated Enthalpy of Sublimation and the Characteristic Binding Energies

Source	O	Na	Mg	Al	Si	P	S	K	Ca	Ti	Cr	Fe	Zn	OH	Mn
E_{sub}	2.58	1.11	1.51	3.41	4.66	4.67	2.87	0.92	1.84	4.90	4.11	4.28	1.35	n.i.	2.94
W10	2.00	2.00	1.54	3.36	4.70	3.27	2.88	0.93	2.10	4.89	4.12	4.34	1.35	1.50	n.i.
Mare basalt	3.57	1.42	1.82	4.35	5.36	n.i.	2.31	1.22	3.60	6.17	5.27	4.43	n.i.	n.i.	2.42
Anorthosite	3.52	1.42	1.83	4.33	4.98	n.i.	n.i.	1.22	3.58	6.17	n.i.	4.49	n.i.	n.i.	n.i.
S-Hem	3.54	1.42	1.54	4.46	5.43	n.i.	2.64	1.22	3.30	5.10	4.37	3.88	n.i.	n.i.	2.42
N. low-Mg	3.57	1.42	1.62	4.66	5.38	n.i.	2.52	1.22	3.49	5.10	4.37	3.61	n.i.	n.i.	2.42

Note. Short forms: E_{sub}—enthalpy of sublimation; n.i.—not included. The characteristic binding energy E_0 is from the adapted Thompson distribution (Equation (7)) used in W10 (Wurz et al. 2010) and this work at an incidence angle of 45°. The error on the database fits caused by different statistics is ±0.1 eV, but two significant digits are given for comparison with W10.

Table 4
Effect of Sulfur Diffusion on Sulfur Sputter Yield from Minerals Irradiated by Solar Wind Speed H and He Ions at Normal Incidence

Group	Mineral		Formula	$Y_{S,0}$ (10^{-4} at/ion)	$Y_{S,diff}$	Δ (1)
Sulfides	Troilite	Tro	FeS	108	2.67	40
	Niningerite	Nng	MgS	132	4.46	30
	Alabandite	Abd	MnS	119	3.18	37
	Brezinaite	Bzn	Cr_3S_4	104	2.23	47
	Wassonite	Was	TiS	65	2.04	32
	Oldhamite	Old	CaS	90	5.69	16
	Daubréelite	Dbr	$FeCr_2S_4$	109	2.40	45

Note. Abbreviations: $Y_{S,0}$—sputter yield without diffusion; $Y_{S,diff}$—sputter yield considering diffusion; Δ—factor of decreased yield due to diffusion ($Y_{S,0}/Y_{S,diff}$).

Table 5
Comparison of Surface Erosion per Incident Atom of Sulfides and Enstatite

	En MgSiO$_3$	Tro FeS	Nng MgS	Unit
S diffusion	...	... 7.5	7.5	10^2 Å^4 at^{-1}
Yield	0.35	0.94 2.00	2.71	amu/ion
Molar mass	100.00	87.91 87.91	56.37	amu
Density	3.20	4.82 4.82	3.22	g cm^{-3}
V/ion	1.82	3.68 7.84	24.80	10^{-27} cm^3/ion
V:V_{En}	1.0	2.0 4.3	14	

Note. Yields are for normal incident SW ions and computed based on the model introduced in Jäggi et al. (2023) without diffusion compared to the same model with a damage-driven diffusion coefficient (Christoph et al. 2022). Ratio in volume equates to depth ratio assuming that two irradiated areas are of equal size.

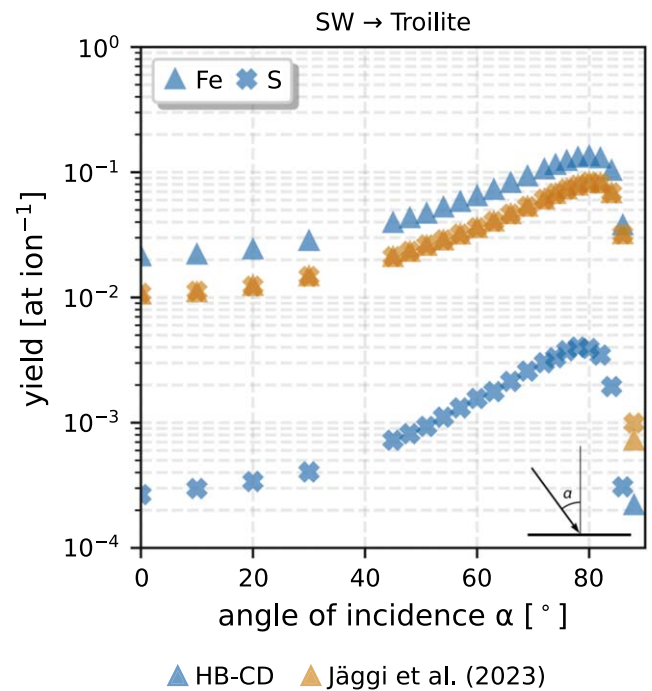## 3.3. Multiply Charged Solar Wind Ions

In nature, SW exposed celestial bodies are subject to simultaneous irradiation of all SW constituents. This includes on average of approximately 96% protons, 4% alpha particles; a few per mil of heavier, multiply charged ions such as O^{6+}–O^{8+}, C^{5+}, and C^{6+}; and rarer constituents such as Ar^{8+}, not exceeding the ppm range (Gosling 2007). SDTrimSP cannot take into account the increase in sputter yield caused by the potential of the multiply charged species (e.g., Aumayr & Winter 2004; Barghouty et al. 2011). However, the contribution to the sputter yield is only significant for He (+40% yield; Szabo et al. 2022a), as, due to their low abundance, the sputter yield for less abundant species would have to be several orders of magnitude higher than for H to become significant. The experimentally confirmed 40% yield increase for He^{2+} on silicates is also consistent with the theoretical 35%–50% increase in yields caused by potential sputtering shown in Table 8 of Killen et al. (2012). Other heavy, multiply charged ions in the SW further increase the sputter yield. They make up about 7.5% of the kinetic yield (compared to the 18.4% kinetic yield contribution of He^+ ions determined by Nénon & Poppe 2020) and are expected to have a noticeable effect on the total yield if included in the simulations. This will be done once their yield increase due to potential sputtering is known (e.g., for multiply charged Ar ions a potential sputtering yield increase of a factor of two was found; Szabo et al. 2018, 2020).


Figure 6. Sputter yields of Fe and S from troilite irradiated by SW ions in the model introduced in Jäggi et al. (2023) compared to the same model with a damage-driven diffusion coefficient of 7.5×10^2 Å^4 at^{-1} (Christoph et al. 2022; HB-CD). Note that sputter yields become stoichiometric when they reach an equilibrium, which is not the case if surface S is depleted by diffusion in addition to being sputtered.
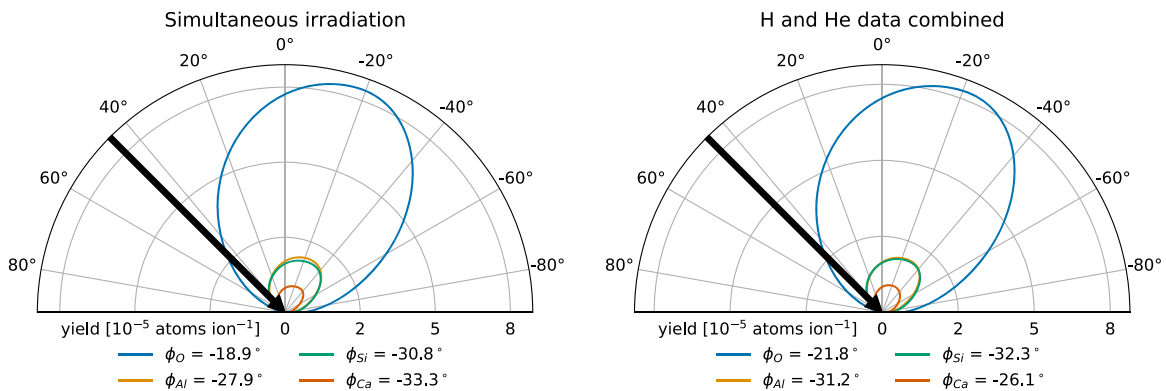
Figure 7. Angular distribution of sputter yield from anorthite ($CaAl_2Si_2O_8$) from combined H and He data (left) compared to simultaneous irradiation by H and He (right). In both cases the H:He ratio is 96:4 and the incident angle is $45°$. Note that the largest difference in tilt angle (ϕ) is for the least sputtered species, Ca, which is assumed to be less heavily depleted in the simultaneous irradiation, causing a larger surface concentration and a more forward-faced ($\alpha < 0$) angular distribution as a consequence.

Table 6
Loss Fractions of Sodium and Oxygen Sputtered from the Hermean Surface

		Mercury		Moon	
	W10	Southern Hemisphere	Northern Low-Mg Terrane	Mare	Highland
O	0.81	0.89	0.89	0.98	0.98
Na	0.72	0.56	0.56	0.87	0.87

Note. W10—Wurz et al. (2010) loss fractions are calculated from integration. Southern hemisphere and northern low-Mg terrane loss data are computed by the database.

3.4. Separate and Simultaneous Irradiation

We compared the sputter yields from simultaneous H and He irradiation modeling with the single irradiation data mixing model applied in SpuBase. We found that the results differ in sputter yield and angular distribution. The mixing model, which adds up data from H and He simulations at a given ratio, results in sputter yields (in atoms/ion) up to 16% lower than the data from simultaneous H and He irradiation. For angular distribution data, the forward tilt (ϕ_{tilt}) and shape parameters (m, n) differ the most, predominantly for species that accumulate in the surface as other species are removed (Figure 7). The energy distributions show no significant dependency on the way the data are obtained, which is expected because the binding energies are identical in all cases. All deviations are small compared to uncertainties within laboratory experiments and smaller than the major effects caused by adjusting binding energies and bulk densities (e.g., Jäggi et al. 2023).

4. Discussion

The binding energies based on the new model introduced in Jäggi et al. (2023) and the molecular dynamics work by Morrissey et al. (2022) imply higher characteristic energies of many of the sputtered particles compared to assuming the tabulated enthalpy of sublimation (Table 3). As a consequence, a larger fraction of ejecta reach escape velocities and may leave the surface for good. This is illustrated in Table 6 for Mercury (W10; southern hemisphere and northern low-Mg terrane) and the Moon (mare, anorthosite), where we compare our results to Wurz et al. (2010). As shown there, lower binding energies for O lead to lower loss fractions (fraction of atoms with velocities that exceed Mercury's escape velocity), and larger binding energies for Na lead to significantly larger loss fractions for Na. Note that an increase in binding energy not only increases the loss fraction but also reduces the sputter yield, as demonstrated for increasingly energetic Na sourced from increasingly complex silicates in Morrissey et al. (2022).

The largest variations in energy distributions, described by the characteristic binding energy E_0 in Table 3, are caused by sulfides. The comparably low enthalpy of formation of sulfides relative to oxides does not result in the same reduction in yield and low-energetic ejecta. On Mercury, transition metals and Ca, Mg, and Fe ejected from sulfides instead of silicates or oxides (i.e., TiS, FeS, and Cr_3S_4 instead of $FeTiO_3$ and $FeCr_2O_4$) make up a significant part of the sputtered particles. This also slightly affects the characteristic binding energy of Ca for Mercury as a whole (assuming that the southern hemisphere represents Mercury's average composition as done in, e.g., McCoy et al. 2018). There, oldhamite (CaS) makes up only 0.5 vol% of the normative surface mineralogy, but $10\times$ more Ca is sputtered than from anorthite (21 vol%). The low-energetic Ca from oldhamite therefore effectively decreases the ejected Ca energy.

The inclusion of diffusion rates in sulfides further increases the sputter yields of the nonsulfur species therein. Overall our simulations suggest that sulfides erode faster than silicates. In the case of troilite (FeS) irradiated by SW ions, the volume depletion ratio of 4.3 relative to enstatite ($MgSiO_3$) is comparable to the factor of 4 found in the Ga^+ experiment conducted by Keller et al. (2013). However, calculating volume or depth changes from SDTrimSP data is just an approximation. Wilson et al. (1999) have shown, for olivine, that the volume of an irradiated surface might instead increase as the mineral is amorphized, counteracting in part the sputter erosion. The significant increase in sputter yield—and presumably erosion rates and volume changes as shown in Table 5—between sulfides and oxides would favor the theory of Mercury's hollows being composed of fast-eroding sulfides (Vilas et al. 2016; Lucchetti et al. 2018, 2021; Barraud et al. 2023). This is only the case if sputtering can outperform desorption and impact processes.

4.1. CIPW Limitations

For reduced surfaces such as Mercury's, computing oxides from the given element abundances as part of the CIPW norm (Section 2.6) requires more O than measured by the Gamma Ray Spectrometer on board MESSENGER (Evans et al. 2012; McCoy et al. 2018). This low abundance of O at the surface is likely a result of near-surface gardening (McCoy et al. 2018). The sputter yields computed in SDTrimSP and reported in SpuBase are valid for the different minerals in equilibrium with the SW. Hence, the surface from which sputtered particles are sourced represents an oxygen-depleted surface.

The northern terrane (McCoy et al. 2018) and northern low-Mg terrane (Table 2; Peplowski & Stockstill-Cahill 2019) have exceptionally large Na_2O, exceeding the amount of Na that can be incorporated into plagioclase. As a result, Peplowski & Stockstill-Cahill (2019) included the surplus Na in a Na-metasilicate (Na_2SiO_3). Another side effect of the large Na_2O content is the absence of olivine, due to there being sufficient SiO_2 to accommodate Mg and Ca into the pyroxenes.

5. Conclusions

SpuBase (Jäggi 2024) was created using the new SDTrimSP model in Jäggi et al. (2023) to generate model inputs relevant for typical surface compositions of the Moon and Mercury. While SDTrimSP calculations can be tailored to intricate mineral compositions and nuances, such customization demands a significant investment of time and effort. SpuBase was conceived to address this disparity. Its purpose is to provide a practical solution for exosphere modelers studying celestial bodies exposed to the SW. This database enables researchers to acquire essential sputter yield inputs for their models without the need to execute the SDTrimSP program. SpuBase is a repository housing SDTrimSP-generated outputs specifically concerning major rock-forming minerals. The results can be validated piecewise, and model assumptions and/or mineral specific deviations can be incorporated with each advancement in the research field. These advances include energy distribution data of sputtered elements and damage-driven diffusion coefficients for nontroilite sulfides, for which no laboratory measurements exist so far. Nevertheless, the underlying model (Jäggi et al. 2023) was shown to reproduce experimental kinetic sputter yields, which gives confidence to the model predictions.

Appendix A
SpuBase Python Class

The most important variables and their use in the class/functions within SpuBase are summarized in Table A1. For a demonstration on how to use SpuBase and on how to recreate the figures shown in this work, please follow the step-by-step Jupyter notebooks included in the database (Jäggi 2024).

Table A1
Class, Functions, and Variables Found in SpuBase in Order of Application

Class	Description
Particles()	Initializes the SpuBase class. Optional booleans: verbose = True—SpuBase tells you what is happening in detail; show_plot = False—hides plots, but the plots are still generated and saved into the output folder.

Function	Description
update_file_format(form="png")	Changes file format of figures to any supported file format. Options are, e.g., svg, jpeg, tiff, and pdf.
update_directory()	Creates a folder in "SpuBase/output" based on casename variable where all csv files and figures are saved. If not run, or if casename is not set, all outputs are written into "SpuBase/output."
update_impactor(impactor)	Changes impactor variable to SW/H/He. Optional variable: changes the SW fraction by setting comp_frac (default: [0.96, 0.04]). Only works if sulfides are not included. See Section 3.4 for caveats.
cipw_norm(at_l, at_frac_l):	Determines and returns the CIPW modal mineral composition (minfrac_df_volume) of the surface based on the atomic fractions (at_frac_l) of the atomic species (at_l). Sets a mineral fraction in weight (minfrac_df_weight) and a modal mineral fraction that can be compared to common CIPW implementation where olivine and plagioclase are not differentiated (minfrac_df_volume_CIPW).
surfcomp()	Sets the modal mineral composition (minfrac_df_volume) of the surface based on a given mineralogy or uses the modal mineral composition from the cipw_norm function if available. Also creates an array of the available mineral names (mineral_a). Optional variables: composition from which the surface composition is determined (comp_df) and its form (form=mol%/ wt%/vol%) to determine minfrac_df_volume.
dataseries()	Creates dataframe of all mineral data. If is_summed_up = True and return_amu_ion = False, the data are combined by calling particle_data_refit. The resulting dataframe is written into a textfile called "{impactor}_{casename}_particle_data.txt."
sputtered_particles_data()	Returns scaled functions for particles from energy and angular distribution data as dataframes (edist_df, adist_df) and the element escape fraction (edist_loss_df), if any. Optional variables: ion incidence (dist_angle = 45) and the energy range of interest (energy_a). If no energy range is defined, a linear energy array in the range 0.1–100 eV is used.
plot_dist(dist='energy')	Plots distribution data, saves image, and returns figure and axis object. *Optional variables:* list of species to be plotted (species_l), the total ion flux (ion_flux) to multiply the yield with, the x-axis, or energy maximum in eV (e_lims) and the plot title (title).
plot_yield()	Plots yield data, savesfigure, and return figure and axis object. *Optional variables:* experimental H/He data as dataframes (exp_H_data, exp_He_data).
systemdensity():	Determines bulk density (in $g\,cm^{-3}$) of the system by computing the density of each mineral from compounds (Table 1) followed by a mass balance of all mineral densities and their modal abundance.

Variable	Description
yield_df	Dataframe containing mineral sputter yield information.
particledata_df	Dataframe containing mineral particle information for angular and energy distribution.
refitparticledata_df	Dataframe containing mineral particle information summed up element-wise and refitted (if more than one mineral).
v_esc	Escape velocity in $m\,s^{-1}$ of irradiated body. Necessary to determine escape fraction.
sulfur_diffusion	Boolean. Turns sulfur diffusion on/off in sulfides (False if impactor is not "SW").
plot_amu_ion	Boolean. Allows to plot total mass yield in amu/ion instead of atomic yields.
is_summed_up	Boolean. If set to False, returns results for each individual species separately.

Appendix B
Sulfur Depletion in Troilite

Sulfur was shown to be excessively depleted under ion irradiation (Christoph et al. 2022). In Figure B1 we show the sample depth profiles of the S:Fe ratio within SpuBase and compare them with the original publication (data taken from Figure 8 in Christoph et al. 2022).
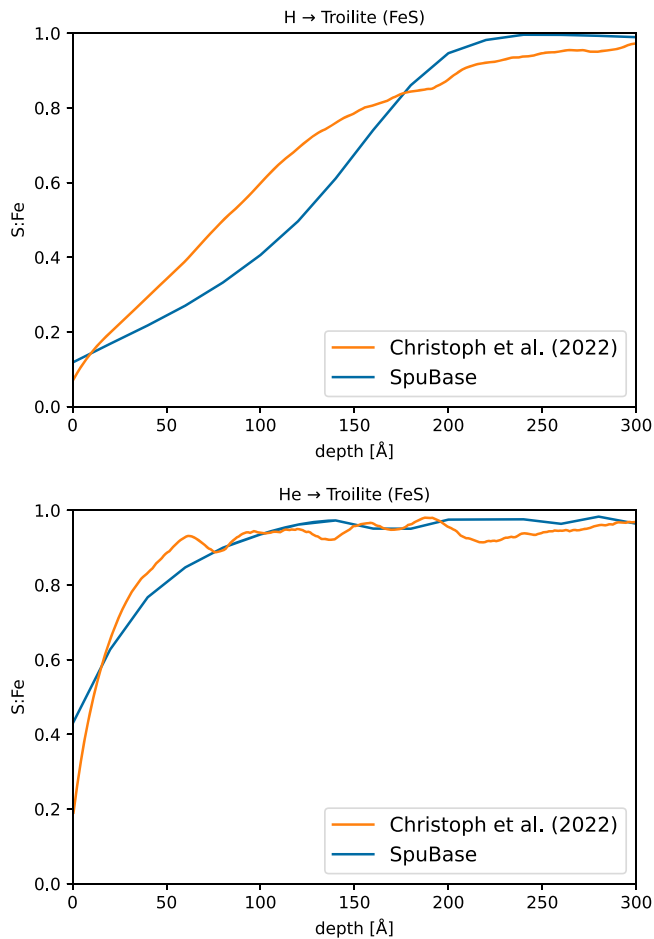

Figure B1. Surface S:Fe ratio in irradiated troilite comparison between this work (blue line) and reference simulation data (orange line; data from Figure 8 in Christoph et al. 2022).

Appendix C
Impactor Energy

The SpuBase data are limited to a single energy for both H and He that corresponds to average SW conditions, or SW speeds of about $440 \, \mathrm{km \, s^{-1}}$ (or $1 \, \mathrm{kev \, amu^{-1}}$; median SW speed between 1998 and 2001 was $412 \, \mathrm{km \, s^{-1}}$; King & Papitashvili 2005). To give the reader an idea of the effect of a ~ 20 times faster or slower SW speed (see data published on OMNIWeb; King & Papitashvili 2005), we computed sputter yields with their energy and angular distributions for 0.5 and 1.5 keV H and for 2 and 6 keV He and compared them to the default energies found in the database, i.e., 1 and 4 keV, respectively.

For H, the change in yield is minor when increasing the impactor energy from low (0.5 keV) to the default (1 keV) and from the default to high (1.5 keV). The largest change in sputter yield is a deviation of $\pm 10\%$ for incidence angles between $30°$ and
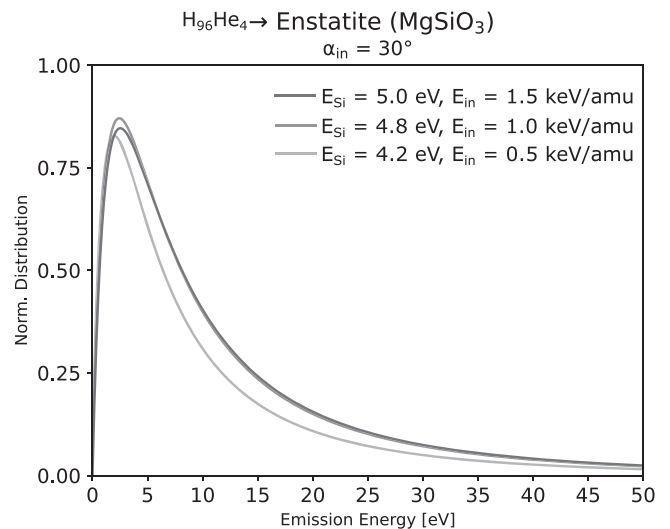
Figure C1. Comparison of the energy distribution of sputtered particles for varying impactor energy E_{in} of SW ions. The shift in the energy distribution at low E_{in} is fully attributed to H, which shows an identical behavior by itself and He on enstatite expressing negligible (<0.2 eV) shifts. The legend contains the element-specific characteristic binding energy E_0, whereas $E_0 \approx 2E_{\mathrm{peak}}$.

$75°$. Note that this change is smaller than the effect of binding energies (Section 4.2 in Jäggi et al. 2023). The polar angular distribution of sputtered particles tends toward the surface with decreasing impactor energy, with the forward tilt decreasing between 5% and 30% (equivalent to about $1°$–$5°$) for normal toward grazing incidence angles between each energy step.

For He, the energies chosen were 2 keV (low), 4 keV (default), and 6 keV (high). The yield increase with each energy step is 20%–30%, more than double the effect on H. The distribution of sputtered particles again tends more toward the surface with decreasing impactor energy; however, there is a different behavior between the two energy steps. Between the low (2 keV) and default (4 keV) energy, the forward tilt angle decreases by 5%–30% with an increasingly grazing incidence, which is also true for H. Between the default (4 keV) and high energy (6 keV) the change at the same incident angles is only a 2%–15% decrease in the forward tilt angle of sputtered particles (Figure C1).

We explain the decrease in the forward tilt angle at larger energies with an increase in penetration depth. Impacting ions with higher energies tend to cause longer collision cascades. With each collision, the influence of the initial impactor trajectory is decreased. The recoils of extensive recoil cascades that make it back to the surface and are consecutively lost therefore become increasingly random in their angular distribution, causing the ejecta to be distributed around the surface normal (i.e., Behrisch & Wittmaack 1991). We would, however, always expect a fraction of sputtered particles to originate from the uppermost layers; therefore, a slight forward tilt of the sputtered particles is expected in any case. This would explain why the high-energy (6 keV) He only shows a small change in the forward tilt angle compared to the default energy of 4 keV.

The energy distribution of sputtered particles only showed a remarkable shift for H impactor energies increasing from 0.5 to 1 keV and only for sputtered Si. The same behavior was also observed for combined H and He irradiation (Figure C1). We expect this to be a combined effect of the shorter collision cascade length and Si having the highest mass and energy of sublimation (4.66 eV, compared to 2.58 eV of O and 1.51 eV of Mg), causing a less prominent high-energy contribution owing

to the rapid loss of the impactor energy limiting the energy transfer. For higher energies, for both H and He, there is no significant shift in the energy distribution peak—energy and scaling fitting parameters from Equation (7) differ by less than 5%—and only the high-energetic tail of the distribution slightly increases.

To conclude, small variations (below 50%) in SW energies do not affect yield and angular distributions beyond uncertainties tied to the sample binding energy and density. We are confident that the database SW sputter yields are largely unaffected by minor SW disturbance.
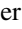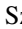
Appendix D
Azimuth Angle Distribution for Sputtered Particles

The azimuth angle for particles sputtered from enstatite ($MgSiO_3$) is shown in Figure D1.
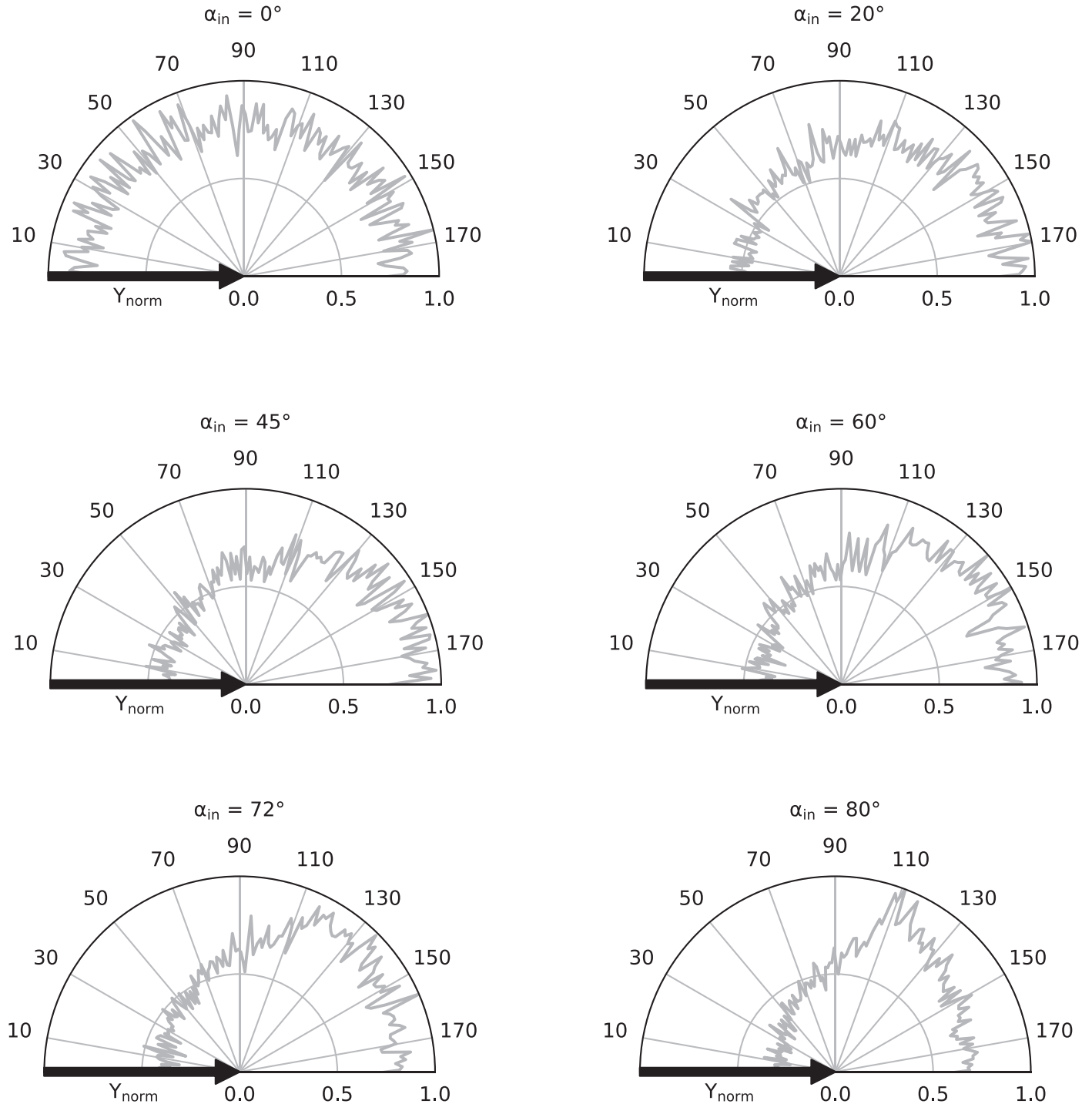
Figure D1. Azimuthal angular distribution of mass sputtered from enstatite ($MgSiO_3$) by 4 keV He^+ at increasing incident angles (α_{in}). Only one hemisphere of the symmetrical distribution is shown. The azimuth angle of the impinging ion (black arrow) is located at $0°$. Note the small remaining fraction of back-sputtered particles at grazing incidence angles ($\alpha_{in} > 45°$).

ORCID iDs

Noah Jäggi ⓘ https://orcid.org/0000-0002-2740-7965
Herbert Biber ⓘ https://orcid.org/0000-0002-9854-2056
Johannes Brötzner ⓘ https://orcid.org/0000-0001-9999-9528
Paul Stefan Szabo ⓘ https://orcid.org/0000-0002-7478-7999
Jonathan Gasser ⓘ https://orcid.org/0000-0002-9237-7088
Friedrich Aumayr ⓘ https://orcid.org/0000-0002-9788-0934
Peter Wurz ⓘ https://orcid.org/0000-0002-2603-1169
André Galli ⓘ https://orcid.org/0000-0003-2425-3793

References

Aellig, M. R., Lazarus, A. J., & Steinberg, J. T. 2001, GeoRL, 28, 2767
Aumayr, F., & Winter, H. 2004, RSPTA, 362, 77
Barghouty, A. F., Meyer, F. W., Harris, P. R., & Adams, J. H. 2011, NIMPB, 269, 1310
Barraud, O., Besse, S., & Doressoundiram, A. 2023, SciA, 9, eadd6452
Behrisch, R., & Wittmaack, K. 1991, Sputtering by Particle Bombardment III: Characteristics of Sputtered Particles, Technical Applications (Topics in Applied Physics, Vol. 64) (Berlin: Springer)
Betz, G., & Wien, K. 1994, IJMSI, 140, 1
Biber, H., Brötzner, J., Jäggi, N., et al. 2022, PSJ, 3, 271
Cartier, C., Namur, O., Nittler, L. R., et al. 2020, E&PSL, 534, 116108
Christoph, J. M., Minesinger, G. M., Bu, C., Dukes, C. A., & Elkins-Tanton, L. T. 2022, JGRE, 127, e2021JE006916
Cintala, M. J. 1992, JGR, 97, 947
Cross, W., Iddings, J. P., Pirsson, L. V., & Washington, H. S. 1902, JG, 10, 555
Cupak, C., Szabo, P. S., Biber, H., et al. 2021, ApSS, 570, 151204
Deer, W. A., Howie, R. A., & Zussman, J. 1992, An Introduction to the Rock-forming Minerals (2nd ed.; Harlow, Essex: Longman Scientific & Technical), 696
Domingue, D. L., Chapman, C. R., Killen, R. M., et al. 2014, SSRv, 181, 121
Dukes, C. A., Chang, W. Y., Famá, M., & Baragiola, R. A. 2011, Icar, 212, 463
Eckstein, W., & Preuss, R. 2003, JNuM, 320, 209
Evans, L. G., Peplowski, P. N., McCubbin, F. M., et al. 2015, Icar, 257, 417
Evans, L. G., Peplowski, P. N., Rhodes, E. A., et al. 2012, JGRE, 117, E00L07
Farrell, W. M., Hurley, D. M., & Zimmerman, M. I. 2015, Icar, 255, 116
Gosling, J. T. 2007, in Encyclopedia of the Solar System, ed. L.-A. McFadden, P. R. Weissman, & T. V. Johnson (Cambridge, MA: Academic Press), 99
Hale, S. A., & Hapke, B. 2002, Icar, 156, 318
Heiken, G. H., Vaniman, D. T., & French, B. M. 1991, Lunar Sourcebook, A User's Guide to the Moon (Cambridge: Cambridge Univ. Press)
Hofsäss, H., & Stegmaier, A. 2022, NIMPB, 517, 49
Housley, R. M., Grant, R. W., Paton, N. E., et al. 1973, LPSC, 4, 2737
Jäggi, N. 2024, nvjaeggi/SpuBase: SpuBase-v1.0 (v1.0). Zenodo, doi:10.5281/zenodo.10783295

Jäggi, N., Galli, A., Wurz, P., et al. 2021, Icar, 365, 114492
Jäggi, N., Mutzke, A., Biber, H., et al. 2023, PSJ, 4, 86
Keller, L. P., Rahman, Z., Hiroi, T., et al. 2013, LPSC, 44, 2404
Killen, R. M., Hurley, D. M., & Farrell, W. M. 2012, JGRE, 117, E00K02
Killen, R. M., Morrissey, L. S., Burger, M. H., et al. 2022, PSJ, 3, 139
King, J. H., & Papitashvili, N. E. 2005, JGRA, 110, 2104
Küstner, M., Eckstein, W., Dose, V., & Roth, J. 1998, NIMPB, 145, 320
Loeffler, M. J., Dukes, C. A., & Baragiola, R. A. 2009, JGRE, 114, E03003
Lucchetti, A., Pajola, M., Galluzzi, V., et al. 2018, JGRE, 123, 2365
Lucchetti, A., Pajola, M., Poggiali, G., et al. 2021, Icar, 370, 114694
McCoy, T. J., Peplowski, P. N., McCubbin, F. M., & Weider, S. Z. 2018, in Mercury: The View after MESSENGER, ed. S. C. Solomon, L. R. Nittler, & B. J. Anderson (Cambridge: Cambridge Univ. Press), 176
Morrissey, L. S., Schaible, M. J., Tucker, O. J., et al. 2023, PSJ, 4, 67
Morrissey, L. S., Tucker, O. J., Killen, R. M., Nakhla, S., & Savin, D. W. 2022, ApJL, 925, L6
Mutzke, A., Schneider, R., Eckstein, W., et al. 2019, SDTrimSP Version 6.00 (IPP 2019-02). Garching: Max-Planck-Institut für Plasmaphysik, doi:10.17617/2.3026474
Nénon, Q., & Poppe, A. R. 2020, PSJ, 1, 69
Nittler, L. R., Boujibar, A., Crapster-Pregont, E., et al. 2023, JGRE, 128, e2022JE007691
Paige, D. A., Siegler, M. A., Harmon, J. K., et al. 2013, Sci, 339, 300
Peplowski, P. N., & Stockstill-Cahill, K. 2019, JGRE, 124, 2414
Pfleger, M., Lichtenegger, H., Wurz, P., et al. 2015, P&SS, 115, 90
Pieters, C. M., & Noble, S. K. 2016, JGRE, 121, 1865
Szabo, P., Weichselbaum, D., Biber, H., et al. 2022a, NIMPB, 522, 47
Szabo, P. S., Biber, H., Jäggi, N., et al. 2020, ApJ, 891, 100
Szabo, P. S., Chiba, R., Biber, H., et al. 2018, Icar, 314, 98
Szabo, P. S., Cupak, C., Biber, H., et al. 2022b, Surfaces and Interfaces, 30, 101924
Taylor, L. A., Pieters, C. M., Keller, L. P., Morris, R. V., & McKay, D. S. 2001, JGR, 106, 27985
Thompson, M. W. 1968, PMag, 18, 377
Vander Kaaden, K. E., & McCubbin, F. M. 2016, GeCoA, 173, 246
Vilas, F., Domingue, D. L., Helbert, J., et al. 2016, GeoRL, 43, 1450
von Toussaint, U., Mutzke, A., & Manhard, A. 2017, PhST, 170, 014056
Weider, S. Z., Nittler, L. R., Starr, R. D., McCoy, T. J., & Solomon, S. C. 2014, Icar, 235, 170
Weider, S. Z., Nittler, L. R., Starr, R. D., et al. 2012, JGRE, 117, E00L05
Weider, S. Z., Nittler, L. R., Starr, R. D., et al. 2015, E&PSL, 416, 109
Wilhelm, R., Deuzeman, M., Rai, S., et al. 2023, NIMPB, 544, 165123
Wilson, C., Muir, T., & Vesenka, J. 1999, in Atomic Force Microscopy/Scanning Tunneling Microscopy 3, ed. S. H. Cohen & M. L. Lightbody (Berlin: Springer), 125
Winslow, R. M., Lugaz, N., Philpott, L., et al. 2020, ApJ, 889, 184
Wurz, P., Fatemi, S., Galli, A., et al. 2022, SSRv, 218, 3
Wurz, P., & Lammer, H. 2003, Icar, 164, 1
Wurz, P., Whitby, J. A., Rohner, U., et al. 2010, P&SS, 58, 1599
Ziegler, J. F., Ziegler, M. D., & Biersack, J. P. 2010, NIMPB, 268, 1818